ACCSCIENCE PUBLISHING

International Journal of Bioprinting

RESEARCH ARTICLE

Integrating machine learning and finite element simulation for interpretable prediction of 3D-printed bone scaffold mechanics

Rixiang Quan, Fengyuan Liu*, and Sergio Cantero Chinchilla*

School of Electrical, Electronic and Mechanical Engineering, University of Bristol, Bristol, United Kingdom

Abstract

An integrated framework combining finite element analysis (FEA) and artificial neural networks (ANN) is presented to enhance the prediction and design of bioprinted scaffolds. By leveraging the strengths of data-driven learning and physics-based simulations, the hybrid approach (ANN + FEA) achieved superior predictive accuracy and generalization compared to standalone approaches. Validation against experimental results demonstrated that a single ANN model yields a relative error of 5.17% when predicting the scaffold's Young's modulus. Incorporating FEA simulation based on ANN-predicted geometry and material properties reduced the relative error to 4.72%, representing an 8.6% improvement. The framework also enables accurate simulation of unseen combinations of printing parameters located far from the experimental data manifold, reducing prediction errors from 14.2% (ANN-only) to 5.7% (hybrid). By integrating predictive modeling, simulation, and data augmentation, this approach offers an efficient pathway for optimizing scaffold designs and accelerating the development of biomaterials with tailored mechanical performance.

Keywords: 3D printing; Artificial neural network; Bone scaffold; Data augmentation; Finite element analysis

***Corresponding authors:**
Fengyuan Liu (fengyuan.liu@bristol.ac.uk)

Sergio Cantero Chinchilla (sergio.canterochinchilla@bristol.ac.uk)

Citation: Quan R, Liu F, Chinchilla SC. Integrating machine learning and finite element simulation for interpretable prediction of 3D-printed bone scaffold mechanics. *Int J Bioprint*. 2025;11(6):327-348. doi: 10.36922/IJB025270257

Received: June 30, 2025
Revised: August 25, 2025
Accepted: September 2, 2025
Published online: September 2, 2025

1. Introduction

Bone tissue engineering involves the development of biological substitutes designed to restore, maintain, or improve tissue function.[1] Central to this field is the design of scaffolds—three-dimensional (3D) structures that mimic the extracellular matrix and provide mechanical and biochemical support for cell adhesion, proliferation, and differentiation.[2] An ideal scaffold should exhibit interconnected porosity to allow for vascularization and nutrient exchange, biodegradability to enable gradual replacement by natural bone, and sufficient mechanical strength to withstand physiological loads during regeneration.[3]

Among various scaffold fabrication strategies, fused deposition modeling (FDM)-based 3D printing has gained significant traction due to its flexibility, cost-effectiveness, and ability to fabricate patient-specific implants with tailored geometry

and porosity.[4] FDM allows layer-by-layer deposition of thermoplastic filaments, enabling rapid prototyping of complex structures with high spatial resolution and reproducibility. Furthermore, it supports a wide range of biomedical polymers, including polycaprolactone (PCL), polyetheretherketone (PEEK), and polylactic acid (PLA).[5]

Polylactic acid has emerged as one of the most widely used materials for scaffold fabrication, owing to its biodegradability, biocompatibility, renewability, and excellent printability.[6] As a widely accepted polymer for biomedical applications, PLA has been extensively adopted in medical devices, resorbable sutures, and implantable scaffolds. Its compatibility with FDM enables the fabrication of complex, patient-specific geometries with tunable porosity and high spatial resolution. However, the mechanical performance of PLA scaffolds is strongly influenced by processing parameters such as nozzle temperature, print speed, layer height, and feed rate.[7] These variables affect both the geometry and stiffness of the printed structure in nonlinear ways. To ensure consistency and performance reliability, especially in customized biomedical applications, predictive models are needed to map processing conditions to scaffold properties.[8]

Traditionally, optimization of these parameters has relied on trial-and-error experimentation, expert knowledge, or statistical methods such as design of experiments and response surface methodology. While informative, these methods are resource-intensive, time-consuming, and poorly suited for high-dimensional design spaces or real-time customization.[9,10] In recent years, machine learning (ML) techniques have emerged as powerful tools for modeling the complex relationships between printing process parameters and scaffold performance.[11] Regression models—including support vector machines, decision trees, random forests, and artificial neural networks (ANN)—have shown great potential in predicting material properties such as tensile strength, Young's modulus, thermal stability, and degradation behavior.[12]

Despite these advances, several limitations remain. First, the direct use of ML to predict mechanical performance, such as Young's modulus or ultimate tensile strength, typically requires a large and diverse dataset obtained through extensive physical experimentation.[13] Such datasets can be difficult and costly to acquire, especially in biomedical contexts where ethical and material constraints apply. Second, many ML models, particularly deep learning approaches, suffer from limited interpretability. These "black-box" models often provide high predictive accuracy without offering insights into the underlying physical mechanisms that govern scaffold performance.[14]

Recent advances have demonstrated the growing potential of integrating finite element analysis (FEA) with ML for optimizing the design and performance prediction of architected materials and scaffolds. For example, Kalina *et al.*[15] proposed the FEANN framework, which embeds physical constraints directly into neural network architectures, allowing for physics-consistent predictions of material responses without explicit constitutive modeling. Their model is trained using automated multiscale data mining and provides efficiency in predicting stress–strain responses of complex hyperelastic materials. However, this framework does not incorporate fabrication parameters or allow for direct design feedback from experimental constraints.[15]

In a similar direction, Peng *et al.*[16] introduced a generative active learning framework (GAD-MALL) that combines 3D convolutional neural networks with FEA to optimize the design of gyroid-based architected implants. Their method excels in high-dimensional, multi-objective optimization, and adapts to clinical constraints such as elastic modulus, yield strength, and printability. The framework achieves notable gains in mechanical performance by exploiting nonuniform gyroid designs and local porosity control, showing excellent agreement between finite element method (FEM) predictions and experimental validation. Nevertheless, this approach focuses on fixed topological families (e.g., triply periodic minimal surfaces) and lacks explicit interpretability or modular prediction steps tied to fabrication conditions.[16]

Another notable line of research by Oladipo *et al.*[17] focuses on optimizing the mechanical performance of re-entrant auxetic metamaterials through a hybrid ML–FEA approach. Their framework integrates experimental characterization of 3D-printed structures, finite element simulation of auxetic deformation under load, and interpretable ML using SHapley Additive exPlanations (SHAP) values to identify dominant geometric features influencing mechanical response. A surrogate model is iteratively corrected using simulation feedback to refine prediction accuracy. This approach offers valuable insight into the structure–response relationship and supports inverse design by highlighting influential geometric descriptors. However, it primarily targets unit cell design within a fixed metamaterial family, and the model relies heavily on empirical geometric encoding rather than direct fabrication parameters. Furthermore, while interpretability is improved through SHAP analysis, the model architecture remains monolithic, limiting modularity and reuse.[17]

Recently, explainable ML approaches have also been introduced for scaffold design to enhance interpretability and provide feature-level insights. For example, Drakoulas

et al.[18] proposed an explainable ML-based framework for bone tissue engineering scaffolds, combining reduced-order modeling with SHAP-value analysis to identify the influence of geometric and material descriptors on mechanical performance. Our modular ANN–FEA framework complements this direction by explicitly integrating filament geometry, material properties, and physics-based simulation to produce interpretable and physically grounded predictions of scaffold stiffness.

Additionally, Dong *et al.*[19] proposed an efficient ML–FEA coupling method to optimize process parameters in laser powder bed fusion for metallic additive manufacturing. Their work addresses the critical challenge of balancing manufacturing-induced thermal effects with final part quality by predicting residual stress and porosity from controllable printing inputs such as laser power and scan speed. The model employs Gaussian process regression and is supported by FEM-based thermal and mechanical simulations, which are used both for training and validation. The study demonstrates significant potential for reducing experimental trial-and-error in metal additive manufacturing (AM) and provides a pathway for process-level optimization. However, this framework is oriented toward process–property prediction at the bulk material level and does not explicitly model the mechanical performance of printed structural architectures (e.g., lattice scaffolds), nor does it incorporate geometric feature learning.[19]

In this study, we introduce a modular hybrid modeling framework (Figure 1) to address the limitations of existing process–performance prediction methods in scaffold fabrication—namely, their dependence on large datasets, limited interpretability, and lack of adaptability. Instead of a monolithic regression model, we decompose the prediction task into three interpretable and physically grounded stages:

(i) ML geometry and material module: Two ANNs (ANN 2 and ANN 3) are used to predict filament geometry (width and height) and the material modulus of PLA, respectively, from the given printing parameters.

(ii) Physics-based module: These predictions are passed into a scaffold-level FEA simulation (Abaqus), which estimates the effective Young's modulus under compressive loading.

(iii) Enhanced ML-based design module: The simulated mechanical outputs are then used to train ANN 1, which predicts optimal printing parameters for desired scaffold stiffness—enabling data augmentation and forward design.

This modular setup mirrors the actual fabrication sequence and ensures that each ANN component aligns with a measurable physical quantity (e.g., scanning electron microscopy [SEM]-derived geometry, tensile-tested modulus). The framework's transparency and adaptability further support generalization under data-scarce or evolving conditions.

The proposed framework offers four key advances over existing approaches. First, it enables modular prediction by decomposing the process–structure–property mapping into interpretable stages, each aligned with physical measurements and simulations. Second, it leverages simulation-guided data augmentation to improve generalization under sparse data conditions, particularly in extrapolative regions of the parameter space. Third, uncertainty-aware modeling is incorporated via ensemble learning and perturbation analysis, allowing confidence-aware predictions for biomedical applications. Finally, the pipeline is designed to be adaptable and extensible, supporting transfer to new materials, scaffold designs, or patient-specific settings by updating only targeted submodules.

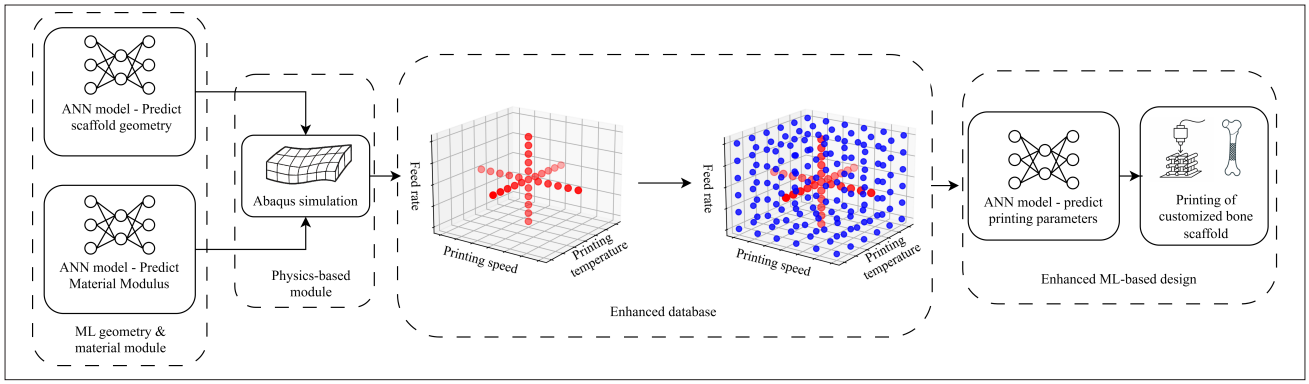

Figure 1. Overview of the proposed framework. Abbreviations: ANN, artificial neural network; ML, machine learning.

The remainder of this paper is organized as follows: **Section 2** details the materials, experimental procedures, and modeling methodology, including the structure of the proposed ANN–FEA framework. **Section 3** presents and discusses the results of model performance and validation. Finally, **Section 4** concludes the study and outlines potential directions for future research.

2. Materials and methods

2.1. Materials and experimental procedures

To quantify how printing parameters affect scaffold geometry—a key determinant of porosity and mechanical properties—detailed measurements of filament dimensions were made using SEM. These experimental data form the foundation for training the geometry-predicting ANN described in **Section 2.3** and are later used to define scaffold models for FEA simulation in **Section 2.4**.

2.1.1. Scaffold design

The scaffolds were designed as grid-like lattice structures, featuring alternating orthogonal filament layers to enhance interconnectivity and mechanical strength. Each scaffold consisted of 20 layers, with filaments in adjacent layers oriented perpendicularly. The nominal pore size, derived from the Computer-Aided Design (CAD) model (Dassault Systèmes, France), was approximately 400 μm, aligning with the optimal range for osteoconduction and vascularization in bone tissue engineering. The designed porosity of the scaffold was approximately 51.1%, calculated based on the ratio of filament volume to total scaffold volume.

Key geometric parameters were held constant across all samples to ensure fabrication consistency: filament diameter (FD) of 0.4 mm, layer thickness (LT) of 0.3 mm, filament gap (FG) of 0.6 mm, and total layer number (LN) of 20. The scaffold dimensions were 10 mm in width and length, and 6 mm in height. Porosity was estimated via a CAD-based volumetric model. The filament layout and key dimensional parameters are illustrated in Figure 2.

2.1.2. Three-dimensional printing of scaffolds

Scaffolds were fabricated using a Prusa MINI+ FDM printer (Prusa Research a.s., Czech Republic) equipped with a 0.4 mm nozzle. PLA "Ecogenius" filaments, purchased from Sigma-Aldrich (Merck Group, USA), were used to produce scaffolds. PLA is a biodegradable, semi-crystalline thermoplastic with a density of 1.24 g/cm^3, a melt flow index of 6.0 g/10 min, an FD of 1.75 mm, a melting point of approximately 144°C, and a Vicat softening temperature of approximately 60°C. Its tensile strength is 65.5 MPa, with a tensile modulus of 3.31 GPa in the machine direction (MD) and 3.86 GPa in the transverse direction (TD).[20] To systematically investigate process–property relationships, three printing parameters were varied:

(i) Nozzle temperature: 180–250°C (five levels: 180; 195; 210; 230; 250°C).

(ii) Printing speed: 100–5100 mm/min (six levels: 100; 300; 900; 1500; 2700; 5100 mm/min).

(iii) Material feed rate: 15–42% (six levels: 15%; 20%; 25%; 30%; 36%; 42%).

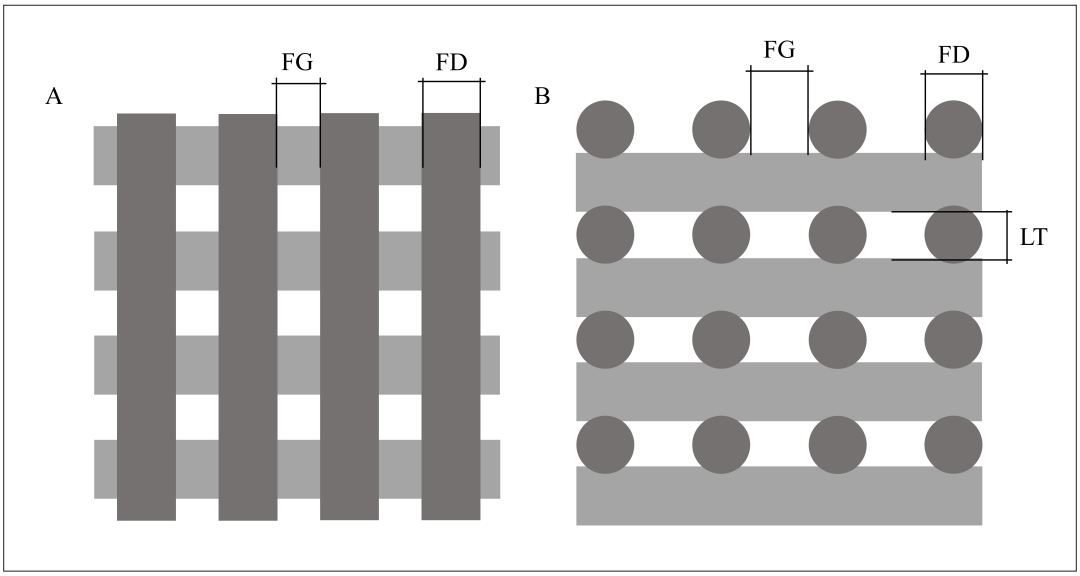

Figure 2. Schematic top view (A) and side view (B) of the printed scaffold structure, illustrating filament gap (FG), filament diameter (FD), and layer thickness (LT).

The selected printing parameters essentially span the typical thermal processing window of PLA, ensuring compatibility with its melting, flow, and solidification behaviors. By covering a broad spectrum of viable printing conditions, these parameters induce substantial variation in filament geometry (e.g., width, height, and inter-layer bonding) and mechanical performance (e.g., Young's modulus and tensile strength).[21] This diversity in output characteristics enables the generation of a rich and discriminative dataset, well-suited for training interpretable and generalizable ML models. From this set, 36 representative parameter sets were selected using stratified sampling, with the goal of covering the printing space evenly across most variable levels.

This resulted in a total of $5 \times 6 \times 6 = 180$ combinations, from which 36 combinations were selected via stratified sampling to cover the design space. Each combination was printed in triplicate, producing 108 scaffolds in total. All other printing parameters that were not the focus of this study (e.g., nozzle size, cooling fan, platform temperature) were kept constant throughout.

2.1.3. Mechanical compressive testing of polylactic acid scaffolds

To evaluate the mechanical performance of the printed scaffolds, uniaxial compression tests were conducted using an INSTRON 3343 universal testing machine (Instron, USA) equipped with a 1 kN load cell. Each scaffold specimen was compressed at a constant crosshead speed of 1 mm/min at room temperature. Force–displacement data were recorded at a sampling rate of 10 Hz.

The compressive Young's modulus was computed from the linear portion of the stress–strain curve, typically within the 5–15% strain range, to exclude the effects of initial seating and nonlinear densification. Stress was calculated based on the projected cross-sectional area, while strain was determined by dividing the crosshead displacement by the initial height of the scaffold.

For each printing parameter combination, three replicate scaffolds were tested. This number was chosen to enable the calculation of mean values and standard deviations, and to quantify fabrication and testing uncertainty, which was subsequently used to validate model predictions.

2.1.4. Mechanical tensile testing of polylactic acid filaments

To assess the intrinsic material properties independent of structural geometry, single-filament tensile tests were carried out. Filament extrusion was initiated at a bed-to-nozzle distance of 0.3 mm, calibrated using standard first-layer gap settings. Filaments were then stretched under uniaxial tension using the same INSTRON system at a crosshead speed of 2 mm/min until failure. The elastic modulus of each filament was extracted from the initial linear elastic region of the stress–strain curve, following the same fitting method used in scaffold compression tests. These filament-level moduli served two purposes: (i) to validate the material modulus predicted by the ANN model, and (ii) to investigate the influence of printing conditions on bulk material behavior. At least three filament specimens were tested per condition.

2.1.5. Scanning electron microscopy

Scanning electron microscopy imaging was performed using a JEOL JSM-IT500 system (JEOL Ltd., Japan) operated at an acceleration voltage of 5.0 kV and a working distance of 14.4 mm. The secondary electron (SE) mode was used to capture both surface and cross-sectional features. Micrographs were acquired under slow scan conditions at magnifications ranging from ×100 to ×1000. Figure 3 shows a representative micrograph, which was used to measure filament width and height, assess layer bonding quality, and identify fabrication defects such as voids or under-extrusion.

Scanning electron microscopy analysis primarily focused on quantifying the geometric structure of individual strands. Cross-sectional images were obtained by fracturing the scaffolds to expose the internal architecture, and the height and width of deposited filaments were measured using ImageJ software (National Institutes of Health, USA).[22] Each filament cross-section was approximated as an ellipse, allowing for a simplified yet representative assessment of strand geometry. These dimensional measurements were subsequently used to validate the ANN-predicted geometry and to calibrate the finite element models.

For each printing parameter combination, three scaffolds were fabricated. Each scaffold was fractured to expose the filament cross-sections, and filament width and height were measured at 20 different locations per scaffold using SEM. For each condition, the reported filament dimensions were obtained by first averaging the 20 measurements for each scaffold, and then averaging the three scaffold-level values to give the final mean.

In addition to geometric evaluation, SEM imaging also provided qualitative insights into interlayer bonding and surface morphology. Process-induced defects such as insufficient fusion, void formation, or surface roughness were identified and used to interpret inconsistencies in mechanical performance and predictive errors within the ANN–FEA framework. The complete experimental

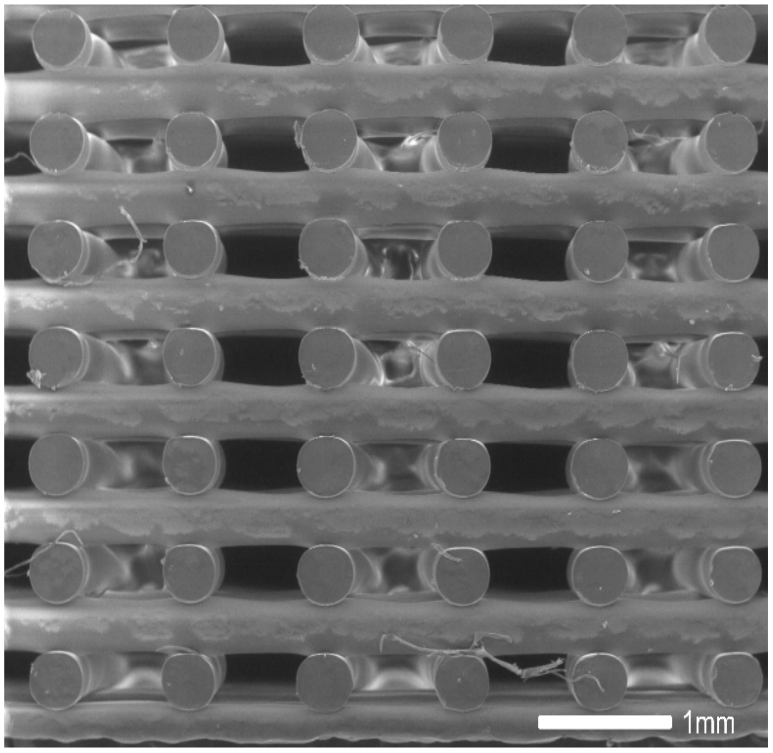

Figure 3. Scanning electron micrograph of the cross-sectional filament layout in a three-dimensional-printed polylactic acid scaffold. Scale bar: 1 mm; magnification: 30×.

workflow, including printing, testing, and image-based analysis, is summarized in Figure 4.

2.1.6. Experimental uncertainty quantification

Repeated tests were conducted for selected printing conditions to evaluate fabrication variability and quantify experimental uncertainty in the measured mechanical and geometric properties. For each selected combination of nozzle temperature, print speed, and feed rate, three scaffolds were fabricated and subjected to the same compression testing protocol. The number of replicates (n = 3) was chosen as a trade-off between statistical robustness and practical throughput, allowing estimation of mean values and standard deviations while managing resource constraints.[23]

The resulting Young's modulus values and filament dimensions (width and height) were analyzed to compute the standard deviation and coefficient of variation for each condition. These metrics characterized the inherent variability arising from machine-level fluctuations and material inconsistencies during the FDM process.[24]

This uncertainty information served a key purpose within the modeling framework: it provided reference bounds for validating ANN and FEA predictions, ensuring that model deviations were interpreted in the context of experimental variability (aleatoric uncertainty).[25]

2.2. Finite element analysis

To complement the geometric dataset and capture intrinsic material variability under different processing conditions, tensile tests were performed on individual PLA filaments. These tests provided ground-truth Young's modulus values for the material-property ANN introduced in **Section 2.3**, ensuring that simulation inputs reflect realistic mechanical properties.

2.2.1. Geometry definition and material properties

Finite element models of the scaffold structures were constructed in Abaqus/Standard to simulate their mechanical response under uniaxial compression. The geometry of each scaffold was defined as a periodic grid-like structure with alternating orthogonal filament layers. Filaments were modeled with approximate elliptical cross-sections, where strand width and height were either experimentally measured (via SEM) or predicted using the ANN model. This elliptical approximation enabled a more

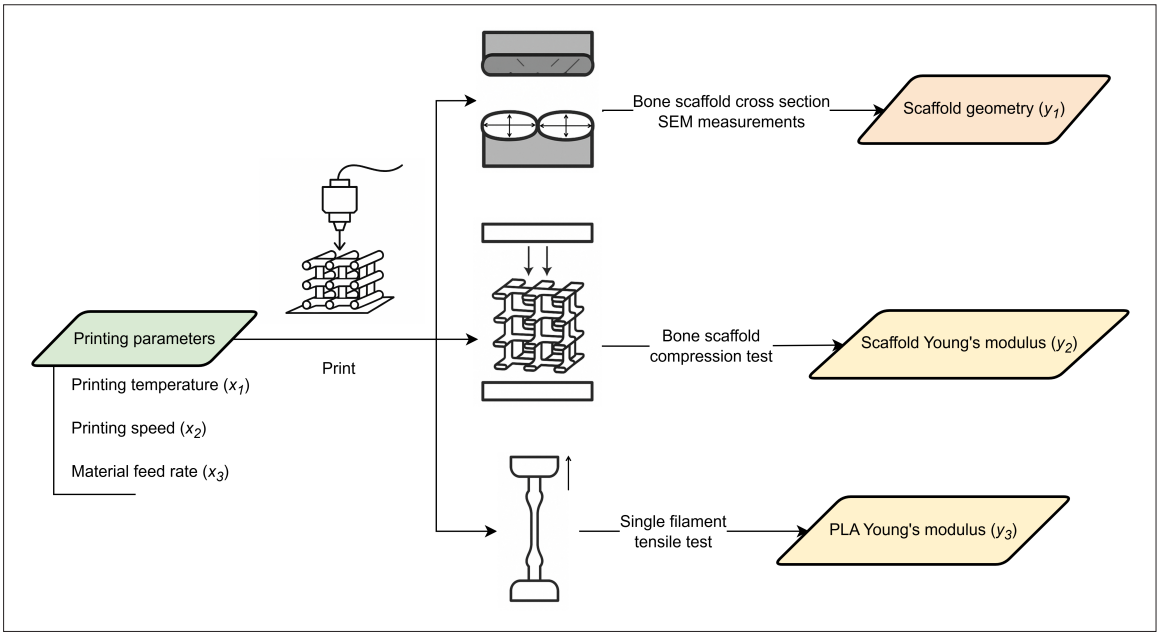

Figure 4. Experimental data collection process, including printing parameters and mechanical property measurement.

realistic representation of printed strand morphology compared to idealized circular or rectangular assumptions.

Each scaffold model comprised multiple filament layers, consistent with the actual printing strategy. The spatial arrangement, filament spacing, and stacking sequence were derived from the original CAD design, ensuring a one-to-one correspondence between the modeled and printed geometries.

Polylactic acid was modeled as a homogeneous, isotropic, and linear elastic material. The Young's modulus was assigned based on ANN-predicted tensile properties of PLA filaments under the same printing parameters used for the corresponding scaffold structure. A constant Poisson's ratio of 0.36 was used throughout.[26]

2.2.2. Mesh convergence study

To ensure the reliability of simulation results and minimize discretization error, a mesh convergence study was conducted on a representative scaffold model.[27] Both linear hexahedral elements (C3D8R) and tetrahedral elements (C3D4) were initially evaluated. Due to the regular scaffold geometry and the dominance of axial loading, C3D8R elements were ultimately selected. These linear hexahedral elements demonstrated higher accuracy in stress prediction and stiffness estimation compared to their tetrahedral counterparts, particularly in structured geometries with predominantly orthogonal filament arrangements. In addition to improved precision, C3D8R elements also offered better numerical stability and reduced element distortion, enabling more efficient simulations without compromising result fidelity.[28]

A series of progressively refined meshes was tested, with element sizes of 0.20, 0.15, 0.10, 0.08, and 0.05 mm. For each mesh level, a fixed compressive load was applied to the scaffold's top surface, and the resulting average vertical displacement was recorded. Mesh convergence was evaluated by tracking the change in displacement across successive mesh refinements. Convergence was considered acceptable when the relative change in top surface displacement between two consecutive mesh levels was less than 5%, a commonly used threshold in similar scaffold and biomedical FEA studies.[29] Based on this criterion, a mesh size of 0.08 mm was selected for subsequent simulations, as it provided a good balance between accuracy and computational efficiency.

2.2.3. Boundary conditions and simulation setup

All simulations were performed under quasi-static, linear elastic conditions using Abaqus/Standard. To replicate the experimental compression tests, the bottom surface of the scaffold model was fully constrained in all translational degrees of freedom. A uniformly distributed vertical 100 N force was applied to the top surface, simulating uniaxial compressive loading. The applied displacement magnitude was selected to remain within the linear elastic regime.

Although inter-filament adhesion in FDM printing is imperfect and influenced by parameters such as cooling rate and filling density, experimental and theoretical studies have shown that, under typical fabrication conditions (e.g., high filling density), interfacial bonding strength becomes relatively stable and has a limited influence on global mechanical performance. Therefore, assuming fully bonded interfaces using tie constraints is a valid simplification when the focus is on comparing stiffness across scaffold geometries.[30] All interfaces between adjacent filaments were modeled using tie constraints to represent fully bonded contact between layers.

The output variables included nodal displacements and maximum stress, from which the effective Young's modulus was derived using the ratio of applied stress to resulting strain. Stress was calculated as the applied force divided by the nominal cross-sectional area, and strain was computed from the displacement normalized by scaffold height.

All simulations were run in batch mode using Python-generated input files, allowing for automatic updates of geometry and material parameters across the design space. This automated setup ensured high-throughput analysis with minimal manual intervention and facilitated direct integration with ANN model predictions.

In FEA simulations of 3D-printed polymer structures, discrepancies between simulated and experimental results can arise from several unmodeled factors. Common sources include imperfect interlayer adhesion and cohesive failure under load, which can reduce effective stiffness compared to an ideal, fully bonded model[31,32]; internal voids and porosity, which act as stress concentrators and reduce the load-bearing cross section[33]; and anisotropic behavior introduced by layer-by-layer deposition, where the build (Z) direction is typically weaker than the in-plane directions.[34,35] Additional differences may occur due to residual thermal stresses or geometric deviations if warpage or shrinkage is not considered.[36]

While some sources of discrepancy between simulation and experiment—such as imperfect layer bonding, anisotropic behavior, or porosity—can exist in 3D-printed materials, these effects are considered minimal in our case for the following reasons. First, the scaffolds are primarily subjected to axial compression, under which layer-to-layer bonding has limited influence on the global mechanical response. Second, the printing path uses continuous filaments arranged in a regular grid, which reduces directional anisotropy. Third, SEM inspection confirmed close agreement with the CAD geometry and revealed no significant internal voids or defects. Therefore, while minor deviations between simulation and experiment are still possible, the FEA model offers a reasonable approximation of scaffold behavior within the bounds of observed experimental variability.

2.2.4. Uncertainty quantification via parameter sensitivity

A perturbation-based analysis was performed to estimate the uncertainty in FEA-predicted Young's modulus due to variability in input parameters. For each simulation case, upper and lower bounds were defined for the key input variables—strand width, strand height, and Young's modulus—based on either experimental standard deviations or ensemble-based ANN predictions.

Instead of systematically perturbing each parameter individually, combinations of minimum and maximum values were applied to generate bounding cases. The corresponding FEA simulations yielded a range of effective stiffness values, representing the potential variation in mechanical performance due to input uncertainty. This approach allowed for a conservative estimate of model output variability without requiring a full factorial or probabilistic analysis.

The resulting modulus range was reported alongside the nominal prediction to provide a confidence interval for each case. These intervals enabled comparison with experimental variability and served to validate the robustness of the simulation framework under realistic fabrication-induced fluctuations.

2.3. Artificial neural network modeling

Based on the experimental measurements in **Sections 2.1** and **2.2**, we trained two ANNs: one to predict filament geometry, and the other to predict intrinsic stiffness from printing parameters. These models form the core of our hybrid framework, enabling forward prediction of structural and material properties required for scaffold-level mechanical simulation.

2.3.1. Model architecture and training

To enable accurate prediction of scaffold-level mechanical performance from printing parameters, two modular ANNs were developed: one to estimate filament geometry (width and height), and the other to predict the intrinsic Young's modulus of the printed PLA material. This decomposition mirrors the physical fabrication sequence and improves interpretability, providing inputs for both validation and downstream FEA.

Each ANN adopts a feedforward structure with three hidden layers containing 256, 128, and 64 neurons, respectively. Layers are activated using rectified linear unit (ReLU) functions, with batch normalization and dropout (rate of 0.2) applied to reduce overfitting. Network weights

were initialized using He-normal initialization to optimize convergence in ReLU-based networks.[37]

Training was performed using the Adaptive Moment Estimation (Adam) optimizer (learning rate: 0.01; batch size: 8), with the mean squared error as the loss function. All input parameters (nozzle temperature, printing speed, and feed rate) and output variables (filament width, filament height, and Young's modulus) were min–max normalized to the [0,1] range. This scaling ensures that all variables contribute proportionally during training and improves the numerical stability of gradient-based optimization.

2.3.2. Data splits and validation process

To rigorously assess the generalization performance of the ANN models while avoiding overfitting and information leakage, we employed a nested cross-validation scheme inspired by He *et al.*[37] Specifically, a five-fold outer cross-validation loop was used to evaluate model performance, with each outer fold holding out eight fixed test samples based on predefined index combinations.

Within each outer training set (28 samples), an inner five-fold cross-validation was performed to tune hyperparameters, including the number of hidden units and the learning rate. This inner loop ensured that model selection was independent of the final test evaluation, a critical requirement for avoiding optimistic bias in performance estimates.

For each outer fold, the ANN model was trained using the optimal hyperparameter set obtained from the inner loop and evaluated on the held-out outer test set. Model development, including weight updates and early stopping, was restricted to the inner training and validation subsets.

Model performance was quantified using the root mean squared error (RMSE) and coefficient of determination (R^2), computed between predicted and experimental values for each target variable (filament width, height, and Young's modulus). The final reported metrics represent the average across all five outer folds, capturing both the accuracy and robustness of the predictive framework.

2.3.3. Hyperparameter optimization

To ensure unbiased model evaluation, hyperparameter tuning was performed within a nested cross-validation framework.[38] For each outer train–test split, a manual grid search was conducted on the inner training folds using five-fold cross-validation to select optimal hyperparameter configurations, thereby preventing information leakage and preserving generalization integrity.[39]

Hyperparameter tuning was conducted using a manual grid search over a constrained search space, including network depth (1–2 layers), number of neurons per layer (5–50), activation functions (ReLU, tanh), optimizers (Adam, Root Mean Square Propagation, Stochastic Gradient Descent), and learning rates (1×10^{-3} to 1×10^{-2}).

Based on average validation performance across inner folds, the best configuration was a shallow feedforward network with a single hidden layer of 10 neurons, which offered a good trade-off between complexity and generalization. This selection is consistent with prior findings that shallow architectures often outperform deeper ones when training data are limited.[39,40] ReLU was chosen as the activation function for its superior gradient flow and convergence efficiency, while a linear output activation was used to retain interpretability in regression tasks.[40] Among optimizers, Adam was selected for its robust and adaptive convergence behavior across diverse tasks.[41]

Additional settings included a learning rate of 0.01, weight decay (L2 regularization) of 1×10^{-4}, mini-batch size of 8, and early stopping with a patience of 30 epochs. These values were selected based on inner-fold validation performance and are supported by empirical studies showing improved generalization with small batch sizes and early stopping in overparameterized settings.[42]

During training, initial models exhibited early signs of overfitting—specifically, validation loss began to increase after 10–15 epochs, despite continued decreases in training loss. While dropout regularization (rate = 0.2) was consistently applied, it was insufficient on its own to prevent this divergence. Hyperparameter optimization, particularly tuning of network width and learning rate, substantially reduced this overfitting behavior and resulted in better alignment between training and validation loss.

Crucially, all hyperparameter optimization was conducted independently within each outer training fold, without access to test data, ensuring that the final test performance metrics reflected true generalization capability under realistic, small-sample experimental conditions.[38]

2.3.4. Uncertainty quantification using deep ensembles

To quantify prediction uncertainty and enhance model robustness, a deep ensemble strategy was implemented. For each train–test split, $M = 10$ independent ANN models were trained using identical architectures and hyperparameters, but with different random weight initializations.[43] The final prediction was reported as the ensemble mean, while the

standard deviation across ensemble members was retained as a confidence measure.

Uncertainty was estimated as the standard deviation of ensemble predictions for each sample, following practices outlined by Rahaman and Thiery,[44] who demonstrated that deep ensembles provide robust uncertainty estimates, especially in data-scarce settings. Wider standard deviations were typically observed in regions of the parameter space with sparse training coverage, such as at extreme values of printing speed or feed rate.

Although the networks shared the same structure and training data, stochastic elements in the training process—including random weight initialization, mini-batch ordering, and the optimizer's inherent randomness—led each model to converge to a different local minimum in the non-convex loss landscape. These variations resulted in non-identical function approximations across the ensemble, particularly under data-scarce conditions. As a result, ensemble variance reflects meaningful epistemic uncertainty—which arises from limited data or model knowledge—rather than numerical noise.[45,46]

Compared to single-model predictions, the ensemble mean produced more stable and accurate results across all splits, while the associated variance served as a reliable indicator of model confidence. These uncertainty estimates were later used to assess the reliability of ANN-predicted geometry and modulus inputs to the FEA simulation pipeline, and to guide targeted data augmentation in low-confidence regions.

2.4. Hybrid artificial neural networks + finite element analysis integration

The ANN-predicted filament geometry and material modulus were used as inputs for finite element simulations of scaffold compression. This final stage of the framework translates predicted sub-structural characteristics into global mechanical properties, directly addressing the paper's objective of process-informed, interpretable scaffold design.

2.4.1. Automated artificial neural network-to-finite element analysis integration pipeline

While single ANN models may suffice for simple regression tasks, they often fail to capture the full process–structure–mechanics linkage. To address this, we propose a modular integration framework that reflects the underlying fabrication logic and enhances interpretability. An automated pipeline is developed to seamlessly link ANN predictions with FEA, enabling efficient simulation of scaffold mechanical properties across a wide range of printing parameters.

Specifically, the pipeline incorporates predicted filament width, height, and Young's modulus from trained neural networks to generate geometry-aware Abaqus input files. This approach addresses a key gap in the existing literature: although many studies attempt to correlate process parameters with mechanical performance, few explicitly resolve the intermediate filament geometry. Our method provides an interpretable bridge from process to geometry to mechanics and delivers a reusable tool for geometry-informed simulation of 3D-printed scaffolds.[46,47]

A Python-based script handles the end-to-end automation, including the insertion of ANN outputs into a predefined .inp file template. Scaffold geometry is defined as a regular grid of elliptical filament cross-sections, with mesh density, material properties, and boundary conditions configured according to the simulation setup described earlier. All geometric and material inputs are dynamically updated based on ANN predictions.

The system supports batch processing of multiple parameter combinations. For each input set, an Abaqus job file is automatically generated, organized into structured output directories, and optionally submitted to a solver queue for parallel execution. Post-processing scripts extract reaction force and displacement data, from which the effective Young's modulus is calculated using standard stress–strain relations. The overall training architecture, including data flow and input/output structure, is illustrated in Figure 5. Building on the experimental data acquisition process shown in Figure 4, this diagram outlines how scaffold geometry and material measurements are used to train neural network models for predictive simulation. Green boxes indicate input parameters; purple indicates ANN models; orange denotes outputs; and pink indicates the FEA simulation module. The three ANN submodels are defined as functions of the printing parameters $x = \{x_1, x_2, x_3,\}$, where:

- $y_1 = f_1(x)$ predicts scaffold Young's modulus based on process conditions;
- $y_2 = f_2(x)$ estimates filament geometry (height and width);
- $y_3 = f_3(x)$ predicts the intrinsic Young's modulus of the PLA material.

A notable example reinforcing the interpretability advantage of such a hybrid framework is provided by Oladipo *et al.*[17] They developed an interpretable ML approach for 3D-printed auxetic metamaterials by integrating experiments, FEA-generated simulations, and ANN modeling. After generating a comprehensive dataset of 8096 geometrically varied honeycomb structures via FEA, they trained a feedforward multilayer perceptron,

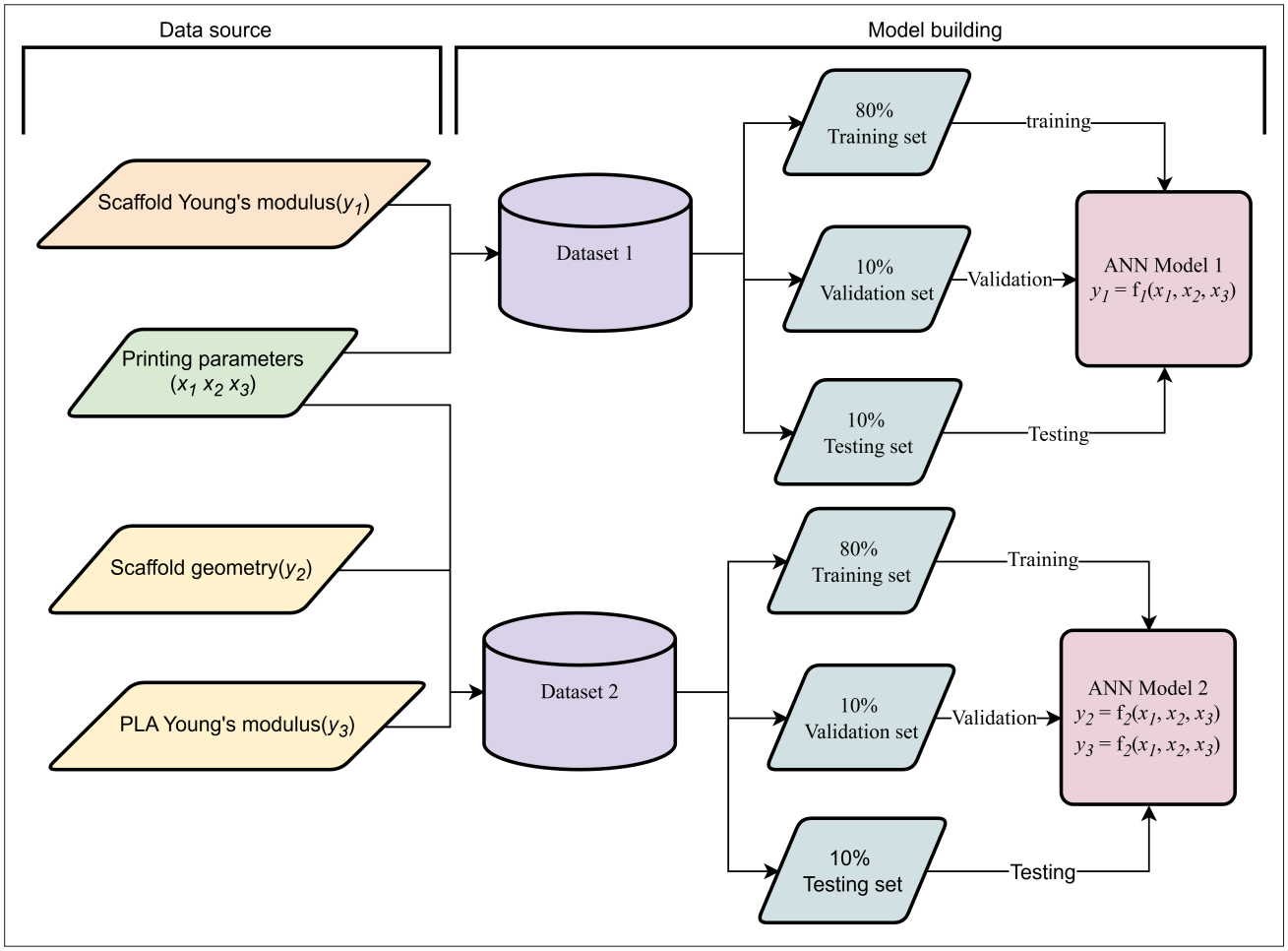

Figure 5. Machine learning model training pipeline, integrating experimental data for predictive modeling.

then applied SHAP analysis to dissect the influence of each geometric parameter on Poisson's ratio predictions. Their findings revealed that slant cell length had the dominant effect, while cell angle and vertical cell length exhibited mixed contributions, and cell thickness had minimal impact. As they conclude, this integrated data-driven framework not only delivered accurate predictive performance but also offered quantitative and interpretable insights into how geometric features influence mechanical response. This study underscores how combining ANN with FEA can elevate both predictive power and transparency in material modeling.[17]

2.4.2. Feedback loop: Augmenting data with simulated results

To address the limitations posed by the small size of the experimental dataset, a data augmentation strategy was implemented by leveraging the integrated ANN–FEA pipeline. Specifically, the ANN models were used to predict geometric and material properties for new combinations of printing parameters, which were then passed into the FEA simulation framework to compute the corresponding effective Young's modulus. These simulated samples formed an extended dataset that approximated additional experimental observations.

This feedback loop enabled the generation of virtual data points in sparsely sampled or previously untested regions of the parameter space, particularly at boundary extremes where physical experimentation may be impractical or resource-intensive. The augmented dataset was subsequently used to retrain or fine-tune the ANN models, improving prediction accuracy and generalization without requiring new physical samples.

While the FEA-based modulus values were not used as direct ground truth for training, they served as a secondary reference to support model evaluation and guide confidence-aware refinement. In addition, uncertainty

estimates from ANN ensembles were cross-checked against the simulation-derived outputs to verify consistency and identify regions with high predictive uncertainty.

Taken together, this hybrid feedback mechanism provides a generalizable solution to data-scarce modelling scenarios where experimental throughput is limited or exhaustive simulation is computationally expensive. The trained ANN models enable near-instantaneous prediction of scaffold geometry and material properties, allowing rapid generation of simulation-ready input files. Compared to manual parameter exploration or full factorial FEA campaigns, this approach substantially reduces iteration time and resource demand, supporting efficient design space augmentation and model refinement. This builds upon the modular training architecture shown in Figure 5, extending it into a full simulation pipeline. The application of trained ANN models to generate FEA input and integrate predictions into scaffold-level simulations is illustrated in Figure 6.

3. Results and discussion

3.1. Predictive performance of artificial neural network submodules

The predictive performance of the ANN models was evaluated using five-fold nested cross-validation, as summarized in Table 1. ANN2, which was trained to predict filament geometry—specifically, height and width—demonstrated strong performance, achieving R^2 values of 0.88 and 0.84, and RMSE values of 0.0181 and 0.0221 mm, respectively. ANN3, which predicts the intrinsic Young's modulus of PLA filaments (from tensile tests), also showed good performance (R^2 = 0.79, RMSE = 0.0259 GPa). These results indicate that geometry and material properties can be accurately inferred from printing parameters when modeled separately.[48]

By contrast, ANN1 was trained in an end-to-end fashion to directly predict scaffold-level modulus from printing parameters. This approach yielded lower predictive accuracy (R^2 = 0.72, RMSE = 0.0338 GPa), likely due to the compounded effects of geometric irregularities, interlayer bonding, and mesostructural variations that affect scaffold mechanics. These complexities make scaffold-level mechanical behavior harder to model without incorporating intermediate structural and material information.[49–51]

Overall, the results support a modular strategy, wherein geometry (ANN2) and material stiffness (ANN3) are predicted separately and then passed to a downstream physics-based FEA simulation. By separating these tasks, each ANN can focus on a narrower, more learnable mapping—improving predictive accuracy, reducing overfitting, enhancing interpretability, and allowing uncertainty to be propagated through the pipeline.[52] This is particularly beneficial in data-scarce settings, where direct end-to-end learning (as in ANN1) risks underfitting or overfitting due to the difficulty of capturing multiscale mechanical interactions.[53]

To better understand how each printing parameter influences the model predictions, we conducted a sensitivity analysis that quantifies the relative contribution of input variables to different outputs. SHAP values, which draw on cooperative game theory, provide a fair, locally accurate, and additive decomposition of a model's prediction, assigning to each input feature its average marginal contribution across all possible combinations.[54,55] In this study, SHAP analysis was performed separately for each ANN submodel: ANN1 (predicting scaffold-level modulus), ANN2 (predicting filament height and width), and ANN3 (predicting filament Young's modulus). In Table 2, SHAP values reveal that printing speed and feed rate are the most influential parameters across all outputs, with feed rate particularly dominating the prediction of

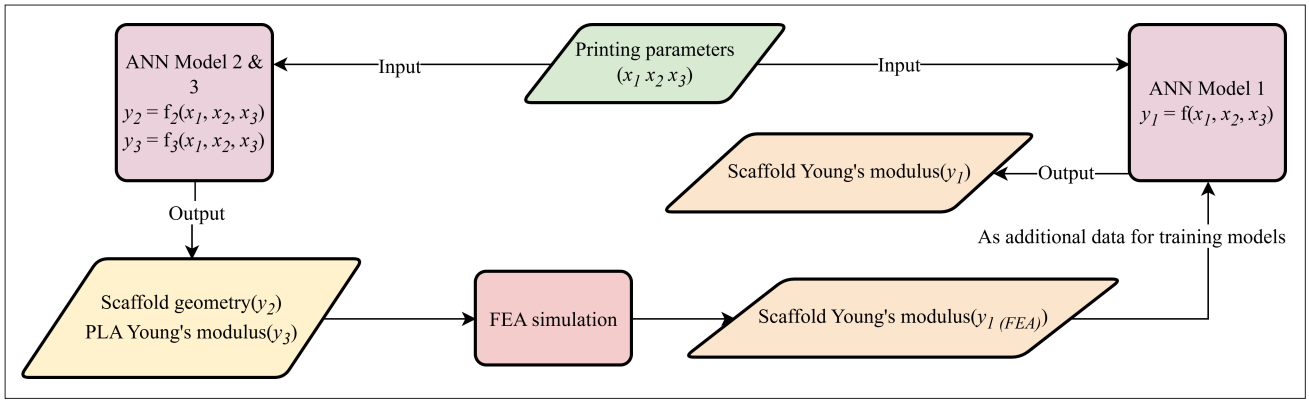

Figure 6. Application of trained models for scaffold property prediction and finite element analysis (FEA) simulation integration. Abbreviations: ANN, artificial neural network; PLA, polylactic acid.

Table 1. Average performance of artificial neural network submodels across five-fold nested cross-validation

Output variable	Predicted by	R^2	RMSE
Height (mm)	ANN2	0.88	0.0181
Width (mm)	ANN2	0.84	0.0221
Filament Young's modulus (tensile test, GPa)	ANN3	0.79	0.0259
Scaffold modulus (compression, GPa)	ANN1	0.72	0.0338

Abbreviation: RMSE, root mean squared error.

filament Young's modulus. Temperature shows relatively minor contributions in all cases.

In addition, a fully dimensionless sensitivity analysis was conducted using a multiple linear regression model applied to FEA-derived outputs (i.e., scaffold stiffness) and their predictors (filament geometry: height and width), all standardized via z-score normalization. By expressing sensitivities in standardized form, one can directly compare the relative influence of each predictor on the FEA model outcome, improving interpretability and comparability across different studies or settings.[56] In Table 3, the estimated coefficients show that feed rate exerts the largest influence across all three outputs, particularly dominating the prediction of scaffold modulus. Temperature has a moderate effect, while printing speed contributes comparatively little.

3.2. Comparison of artificial neural network, finite element analysis, and hybrid artificial neural network–finite element analysis predictions

To evaluate the performance of the proposed two-stage framework, we compared the predicted Young's modulus values from three sources:

(i) ANN: A direct ANN-only model that maps printing parameters (temperature, speed, and feed rate) to scaffold-level Young's modulus. This end-to-end approach does not explicitly model intermediate geometry or material properties and learns purely from experimental data.

(ii) FEA_ANN: A two-stage hybrid model where printing parameters are first input into two ANN submodels to predict filament geometry (width and height) and filament material modulus. These predicted values are then used as inputs to a finite element simulation to compute scaffold modulus.

(iii) FEA: This model uses the same ANN-predicted filament geometry as FEA_ANN but assigns a fixed material modulus of 3500 MPa, based on manufacturer specifications for PLA filament.

(iv) Experiment: Scaffold modulus was measured from compression tests. For each printing condition, three replicate samples were tested, and the mean and standard deviation are reported.

Figure 7 presents the results across three major printing parameters: subfigure (A) corresponds to nozzle temperature, (B) to printing speed, and (C) to feed rate. Shaded regions represent one standard deviation: ensemble-based epistemic uncertainty for ANN and FEA_ANN, and repeatability-based aleatoric uncertainty for experimental data.

To quantify the robustness and statistical variability of ANN predictions, we employed a deep ensemble strategy. Each model was trained 10 times with different random seeds, and the prediction results were aggregated to compute the mean and standard deviation for each test sample. These prediction intervals (mean ± standard deviation) are visualized as error bars in Figure 7. This ensemble-based uncertainty quantification reflects the

Table 2. Average SHapley additive exPlanations values indicating the contribution of printing parameters to each predicted output variable

Input variable	Height	Width	Filament Young's modulus	Scaffold modulus
Printing temperature	2.4×10^{-2}	3.3×10^{-2}	2.8×10^{-2}	1.5×10^{-2}
Printing speed	5.0×10^{-2}	5.7×10^{-2}	4.1×10^{-2}	3.7×10^{-2}
Feed rate	3.8×10^{-2}	5.9×10^{-2}	8.1×10^{-2}	2.1×10^{-2}

Table 3. Standardized regression coefficients from dimensionless sensitivity analysis of printing parameters on each predicted output variable

Input variable	Height	Width	Scaffold modulus
Printing temperature	6.0×10^{-3}	8.0×10^{-3}	1.6×10^{-2}
Printing speed	4.0×10^{-3}	2.0×10^{-3}	8.0×10^{-3}
Feed rate	1.1×10^{-2}	1.3×10^{-2}	3.0×10^{-2}

epistemic uncertainty arising from training stochasticity and provides insight into the stability and generalizability of the model across multiple runs. For the experimental measurements, the error bars likewise represent the mean ± standard deviation obtained from repeated testing, with three scaffold specimens fabricated and tested per printing condition. These experimental bands, therefore, reflect the aleatoric uncertainty associated with fabrication and measurement variability.

The directly predicted modulus from ANN showed good consistency with experimental data, with most values falling within the experimental standard deviation. The modulus values obtained through FEA simulation using ANN-predicted geometry and material properties also aligned reasonably well with experimental results, albeit with slightly higher variance. Notably, the original modulus values computed via direct FEA using measured scaffold geometry and a fixed PLA material modulus of 3500 MPa (as reported by the manufacturer) show systematic overestimation, particularly at higher feed rates and lower print speeds. This is likely because the assigned elastic modulus—by the manufacturer—does not account for local defects or thermal degradation arising from suboptimal printing conditions, such as weak interlayer bonding or residual porosity. These process-induced imperfections can substantially reduce the effective stiffness of the printed material in practice.[30] In contrast, the ANN-informed approach uses material property predictions that reflect the influence of process conditions,

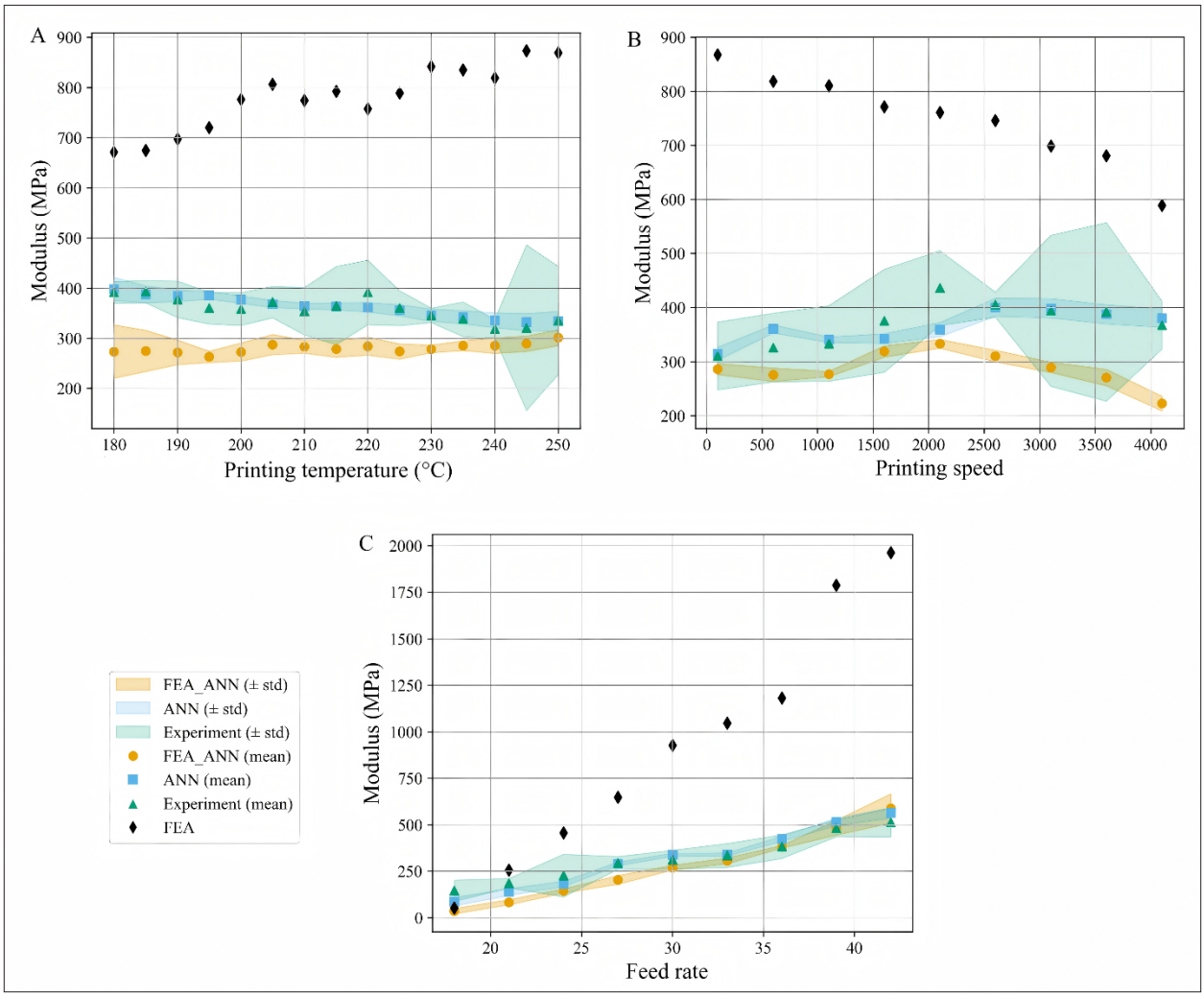

Figure 7. Modulus versus (A) printing temperature, (B) printing speed, and (C) feed rate. Each subplot compares the mean and standard deviation (std) of artificial neural network predictions, finite element analysis (FEA) simulations, and experimental results. Notably, FEA-only results show higher variability, especially under increasing feed rate.

leading to more accurate stiffness estimation when used in FEA simulations.

To quantify uncertainty, we distinguished between two sources: (i) Epistemic uncertainty, which arises from model variability due to limited data, was estimated using a deep ensemble of 10 independently trained models. Prediction error bars in Figure 7 reflect the standard deviation of these ensemble predictions. (ii) Aleatoric uncertainty, caused by fabrication and measurement variability, was captured via three repeated physical tests per printing condition. The resulting experimental standard deviation is shown as green shaded bands, reflecting the repeatability of the physical experiments.

The FEA-predicted scaffold moduli show close agreement with experimental measurements in the elastic regime, as shown in Figure 8. Residual differences are small and fall within the experimental variability, mainly due to minor geometric imperfections or interfacial defects that are not explicitly modeled. This validation confirms that the FEA framework is reliable for generating synthetic samples to support data augmentation.

Uncertainty plays a critical role in evaluating the reliability and generalizability of both data-driven and simulation-based models. In this study, we explicitly address two types of uncertainty:

(i) Aleatoric uncertainty, arising from inherent variability in the fabrication and measurement process, was quantified through repeated experiments. Standard deviations in filament dimensions and scaffold modulus were computed across replicates to capture this stochastic variability.

(ii) Epistemic uncertainty, stemming from limited training data and the model's generalization capacity, was captured via deep ensembles. By training 10 independent ANN models per split with different initializations, the standard deviation across predictions served as an empirical measure of model confidence.

To propagate these uncertainties, we constructed upper and lower bounds for key inputs—geometry and material modulus—based on ensemble variance and experimental statistics. These bounds were passed through the FEA module to generate prediction intervals for the scaffold's Young's modulus.

Notably, larger ensemble variance consistently coincided with input conditions far from the training distribution, such as extreme feed rates or high print speeds. These regions also exhibited larger discrepancies between model predictions and experimental measurements, validating ensemble variance as a useful proxy for model reliability.

This uncertainty-aware hybrid pipeline thus goes beyond point estimates to offer interval-based predictions that better reflect true confidence levels—an essential

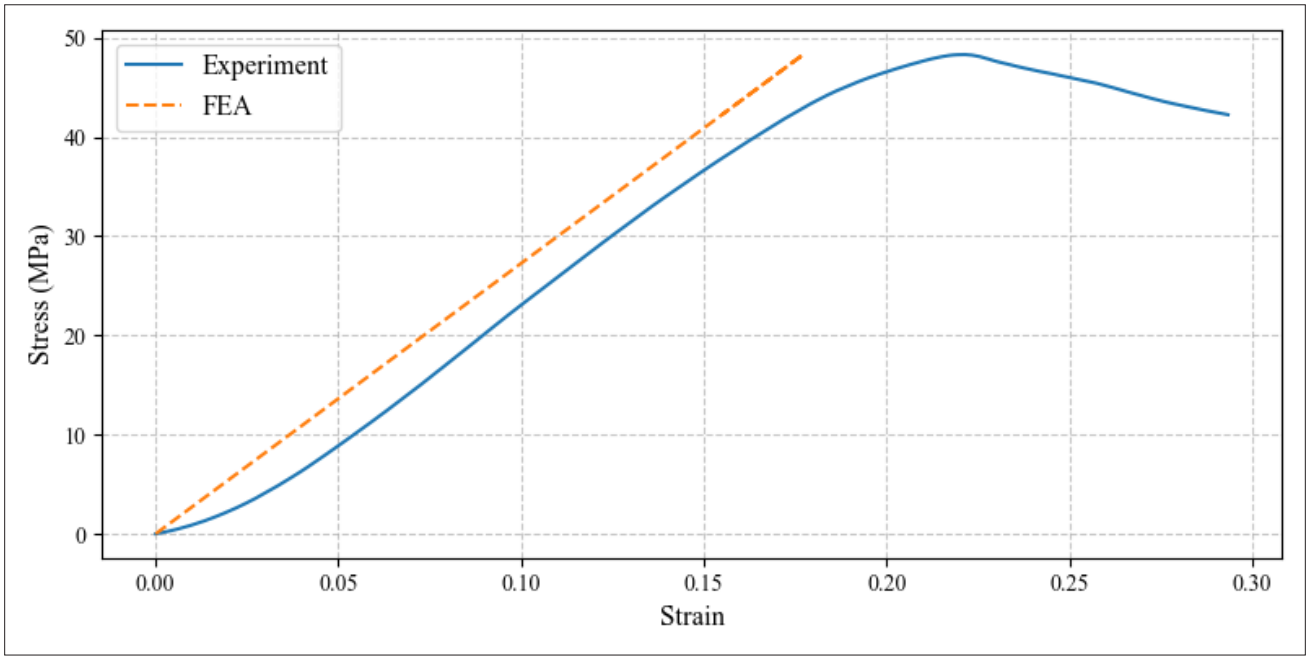

Figure 8. Comparison of experimental and finite element analysis (FEA) stress–strain curves.

feature for biomedical applications, where overconfident errors can carry clinical risk.

While the proposed approach adopts relatively simple ensemble-based and perturbation-based methods to quantify epistemic uncertainty, future work may benefit from integrating more principled uncertainty estimation frameworks. For example, Bayesian deep learning techniques—such as Monte Carlo Dropout or variational inference-based Bayesian neural networks—offer a formal way to capture uncertainty through posterior weight distributions.[57] These methods have been successfully applied in biomedical modeling and are considered strong alternatives to standard ensembles. Similarly, probabilistic FEA frameworks (e.g., stochastic FEA or polynomial chaos expansion) can explicitly propagate parameter uncertainty into mechanical outputs, enabling confidence bounds on predicted stiffness.[58] Incorporating such techniques could enhance the robustness and trustworthiness of hybrid ML–FEA pipelines.

3.3. Extrapolation performance in sparsely sampled regions

This section evaluates the extrapolation capability of the hybrid FEA–ANN model in sparsely sampled regions of the design space, using experimental measurements as the benchmark. Relying solely on physical experiments to explore the full scaffold design space is both time-consuming and costly, making it infeasible to cover every combination of printing parameters. As a result, many parameter combinations remain unseen by a purely data-driven model, which undermines its predictive reliability for new designs. The hybrid ANN–FEA modeling approach is introduced to address this challenge by leveraging physics-based simulations to supplement sparse experimental data. By generating simulation-informed predictions for parameter sets that were never physically tested, the hybrid framework expands the effective dataset and provides better generalization under data scarcity. In essence, FEA acts as a virtual testing ground for rare or extreme conditions, allowing the ANN to maintain accuracy in regions of the design space that would otherwise be beyond its experience.[59]

To demonstrate the benefits of this hybrid strategy, we evaluated the model on 15 scaffold samples with printing parameters deliberately excluded from training. These samples were designed to vary one parameter at a time—temperature, feed rate, or printing speed—while keeping the other two fixed. As summarized in Table 4, the temperature ranges from 190 to 210°C (in 5°C increments), the feed rate varies from 16% to 24% (step size of 2%), and the printing speed ranges from 800 to 1600 mm/min (step size of 200 mm/min). These configurations target boundary or underrepresented regions of the parameter space, allowing for evaluation of the model's extrapolation capability beyond the training distribution.

The Young's modulus was predicted directly by the ANN model and compared with values computed through FEA simulation based on ANN-predicted geometry and material properties. As shown in Table 4, an average relative error of approximately 14.2% was observed for the ANN-only predictions, with errors exceeding 15% in several cases. In contrast, the hybrid FEA+ANN approach achieved significantly improved prediction accuracy, reducing the mean relative error to 5.7%. These results highlight the advantage of incorporating physics-based simulation into the prediction pipeline, particularly when predictions are made beyond the boundaries of the training distribution.[59,60]

These evaluations were performed using the same trained ANN models described in **Section 3.2**; no retraining or fine-tuning was conducted. This setup ensures that the observed improvements in performance are solely attributable to the integration of FEA, rather than any modification of the network. The performance gap can be attributed to several factors. First, the ANN was trained on a relatively sparse dataset, making it difficult to learn accurate mappings in poorly sampled regions. Second, scaffold mechanics are governed by complex, nonlinear interactions among printing parameters (e.g., feed rate affects both deposition volume and cooling behavior), which are difficult to capture with purely data-driven models in extrapolative regimes. Finally, while ANN models interpolate well within the training domain, their reliability declines when predicting outputs for inputs that deviate significantly from those seen during training. These limitations underscore the importance of incorporating physics-based simulations such as FEA to

Table 4. Comparison of artificial neural network model performance with and without simulation-informed data augmentation

Parameter variation	Temperature (°C)	Speed (mm/min)	Feed rate (%)
Varying temperature	190–210 (step = 5)	1200	20
Varying printing speed	200	800–1600 (step = 200)	20
Varying feed rate	200	1200	16–24 (step = 2)

bridge such gaps and maintain predictive fidelity under novel design conditions.[61,62]

To further assess the trend consistency of the prediction models, we visualized the variation in scaffold modulus across three key process parameters: printing speed, feed rate, and nozzle temperature. As shown in Figure 9, subfigures (A), (B), and (C) correspond to the effects of printing temperature, speed, and feed rate, respectively. The predicted modulus from the ANN (blue dashed line) deviates noticeably from experimental trends (orange points), particularly at the extremes of the parameter range. In contrast, the hybrid FEA+ANN predictions (green dashed line) track the experimental data more closely and reproduce expected monotonic relationships, such as the increase in modulus with feed rate and the mild decline with increasing temperature. These findings highlight not only the higher accuracy of the hybrid framework but also its improved ability to generalize physical trends beyond the training data domain.[17,63] This indicates that including simulation-augmented data improves the model's generalization and extrapolation capability.

These results complement the experimental validation in **Section 3.2** and further support the rationale for integrating FEA-based data into the hybrid framework, particularly for exploring regions of the design space beyond the original experiments.

3.4. Data augmentation via simulation and feedback loop

To evaluate the impact of simulation-informed data augmentation on model performance, we trained two versions of the ANN model to predict scaffold Young's

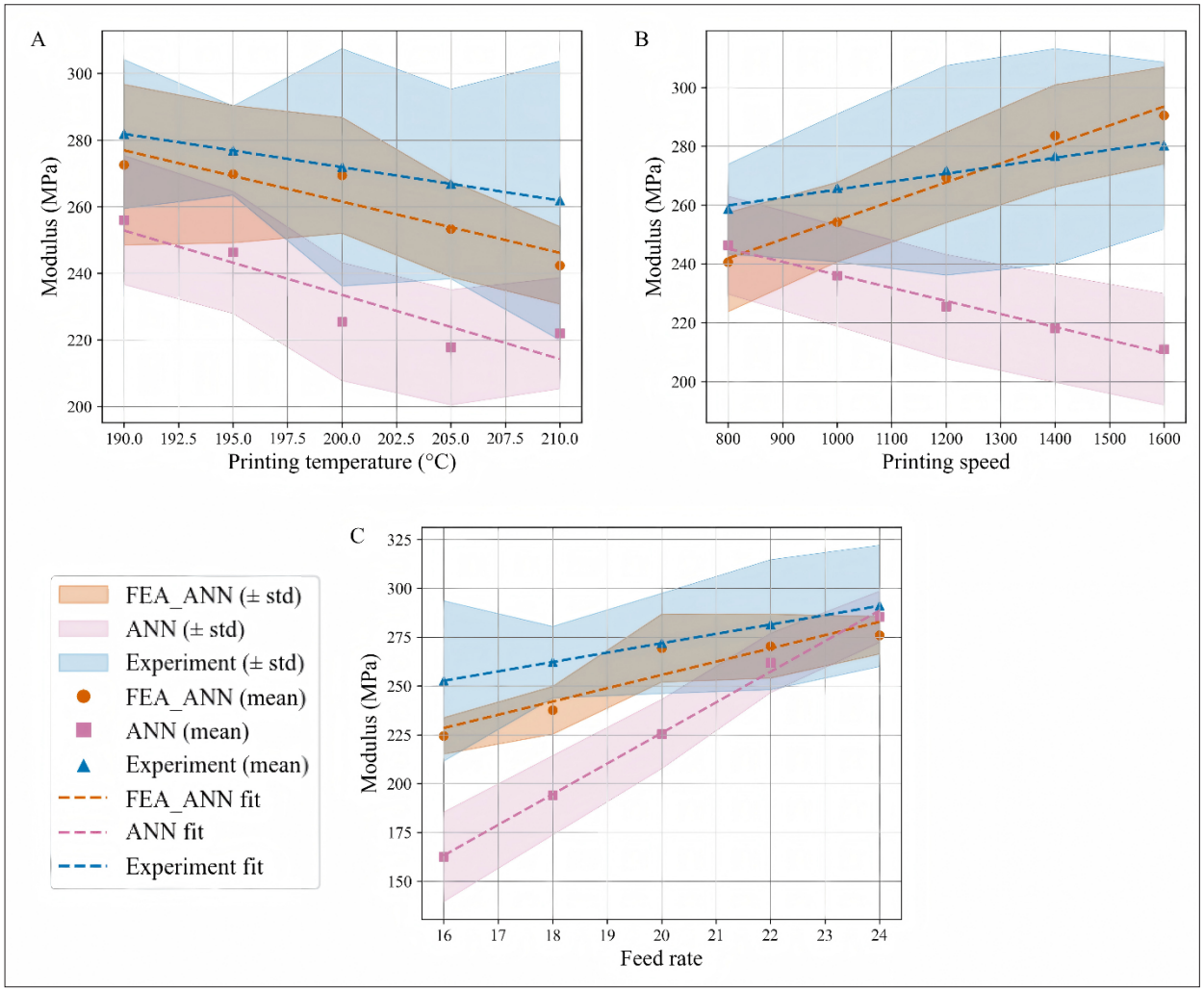

Figure 9. Comparison of predicted and measured Young's modulus under varying (A) printing temperature, (B) printing speed, and (C) feed rate. Dashed lines indicate linear trends for ANN-only (blue), experimental (orange points), and hybrid FEA+ANN predictions (green). The hybrid approach consistently tracks experimental trends more closely. Abbreviations: ANN, artificial neural network; FEA, finite element analysis.

modulus using only printing parameters as input (i.e., ANN3). The first version was trained exclusively on the original experimental dataset. The second version incorporated additional samples to enrich the training distribution. Specifically, 30 new parameter combinations were sampled using Latin Hypercube Sampling (LHS) across the full design space (temperature: 180–250°C; feed rate: 15–42%; printing speed: 100–5100 mm/min). These points were selected to fill underrepresented regions and ensure minimal overlap with existing data. For each LHS-generated point, filament geometry and material properties were predicted using the trained ANN models, and scaffold-level modulus was computed through FEA, resulting in a set of synthetic scaffold samples.

In the present study, we employed a stratified sampling strategy in combination with LHS to achieve uniform initial coverage of the printing parameter space, within the constraints of limited experimental resources. This approach yielded a balanced and interpretable dataset for model training, minimizing sampling bias toward any particular region of the design space. Although effective for the purposes of this study, alternative strategies based on active learning—such as Bayesian optimization or uncertainty-driven sampling—may offer improved data efficiency by adaptively targeting regions with sparse coverage or high predictive uncertainty. While such techniques were not implemented here, they represent a promising direction for future work aimed at accelerating the exploration and optimization of scaffold design spaces.

This combined dataset—consisting of experimental and FEA-augmented samples—was used to train a new ANN model from scratch. As shown in Table 5, both models achieved strong performance on a held-out test set. The ANN trained on experimental data alone yielded a mean absolute error (MAE) of 0.0338 GPa and a relative error of 5.17%. After incorporating simulation-derived data, the MAE was reduced to 0.0283 GPa, and the relative error dropped to 4.72%. These improvements, though modest, indicate that the hybrid ANN–FEA framework can provide valuable generalization benefits by enriching the training distribution, particularly in regions underrepresented in physical experiments.[64,65]

Although the improvement in held-out test performance shown in Table 4 appears modest—reducing the MAE from 0.0338 to 0.0283 GPa—this reflects the fact that the test set is located close to the original experimental data. Given that both training and testing remained within a relatively narrow region of the design space, the benefits of simulation-informed augmentation are partially masked. The true strength of this approach lies in its ability to support extrapolation beyond the training distribution.[66] As demonstrated in **Section 3.3**, for unseen combinations of printing parameters located far from the experimental data manifold, the hybrid ANN–FEA framework achieved substantially lower prediction errors compared to direct ANN models (5.7% vs. 14.2%). This improvement arises because physics-guided data augmentation enriched the training distribution across a wider design space, improving reliability under novel or extreme conditions. These findings suggest that even small test-set improvements may understate the broader generalization gains enabled by simulation-based feedback.

4. Conclusion and future work

This paper presents a modular and interpretable framework that integrates ANN with FEA to predict the mechanical properties of 3D-printed PLA bone scaffolds. By decomposing the prediction process into geometrical, material, and structural levels, the framework supports data-efficient modeling, uncertainty quantification, and enhanced generalization. The key novel contributions are:

(i) Modular prediction pipeline: We proposed a physics-informed, interpretable framework that mirrors real-world scaffold fabrication. It comprises separate ANN submodels for geometry and material property prediction, which feed into a scaffold-scale FEA simulation. This modularity enables validation at each step and simplifies model updating or reuse.

(ii) Simulation-guided data augmentation: We demonstrated how integrating FEA simulations into the training loop augments sparse experimental datasets, enhancing model generalization. In data-scarce regions, the hybrid ANN–FEA approach reduced prediction error from 14.2% (ANN-only) to 5.7% and improved extrapolation performance beyond the training domain.

(iii) Uncertainty-aware modeling: We incorporated deep ensembles and perturbation-based FEA analysis to estimate epistemic and aleatoric uncertainty, offering confidence bounds for predicted scaffold stiffness. This supports risk-aware predictions in biomedical applications.

Table 5. Comparison of artificial neural network model performance with and without simulation-informed data augmentation

Training data	MAE (GPa)	Relative error (%)
Experimental only	0.0338	5.17
Experimental + FEA	0.0283	4.72

Abbreviations: FEA, finite element analysis; MAE, mean absolute error.

(iv) Adaptability and extensibility: The proposed pipeline is reusable and adaptable to new materials, scaffold designs, and clinical requirements. By retraining only relevant ANN submodules, the framework can support multi-material or patient-specific optimization scenarios.

Although the framework demonstrates good predictive performance, it represents a preliminary implementation primarily intended to test feasibility and interpretability under constrained data conditions. This study, therefore, serves as a foundational step toward the development of more generalizable and versatile scaffold design models. Several aspects remain to be expanded in future work. First, this study focuses on short-term mechanical responses of PLA scaffolds under uniaxial compression, without incorporating biological performance factors such as biodegradation, permeability, or cell–scaffold interactions. Second, although the modular structure of the framework supports adaptability, the current implementation has only been applied to a single material system (PLA) and a regular grid architecture. To expand the scope and applicability of the framework, future work is being considered in:

(i) Incorporating advanced material models in the FEA, including poroelastic or viscoelastic constitutive models to represent scaffold behavior under physiological loading and over time.

(ii) Improving data efficiency via active learning strategies—such as Bayesian optimization or uncertainty-guided sampling—to adaptively select new samples in underexplored or high-uncertainty regions, improving efficiency in data acquisition and model refinement.

(iii) Extending to multi-objective optimization by incorporating additional mechanical and biological elements in the objective function.

(iv) Adapting to new materials and architectures through transfer learning techniques: extending the trained models to other biopolymers (e.g., PCL, PEEK) or scaffold topologies (e.g., gyroid, triply periodic minimal surfaces) by leveraging knowledge transfer across related tasks.

(v) Integrating inverse design algorithms: coupling the predictive framework with inverse design methods to enable automated scaffold optimization toward desired mechanical and biological performance.

Acknowledgments

The authors would like to thank Mr. Tom Barnes and Ms. Amy Bland for their technical assistance with 3D printing and mechanical testing at the University of Bristol. We are also grateful to our colleagues Dr. Weiting Xu, Dr. Yi Huang, and Dr. Yan Xu for their constructive discussions and support throughout the development of this research. Special thanks are extended to Dr. Aydin Nassehi, Professor Ben Hicks, and Dr. Qunfen Qi for their academic guidance and inspiration. Rixiang Quan acknowledges the unwavering encouragement and support from his family, especially Qin Yingli, Quan Xin'an, and all those who have supported him along the way.

Funding

This work was supported by the Engineering and Physical Sciences Research Council Impact Acceleration Account 2022–2026 (EP/X525674/1).

Conflict of interest

Fengyuan Liu serves as the Editorial Board Member of the journal but was not involved in the editorial or peer-review process conducted for this paper, either directly or indirectly. The Other authors declare no competing interests.

Author contributions

Conceptualization: Fengyuan Liu, Rixiang Quan, Sergio Cantero Chinchilla
Data interpretation: Sergio Cantero Chinchilla
Formal analysis: Rixiang Quan
Funding acquisition: Fengyuan Liu
Investigation: Rixiang Quan
Methodology: Fengyuan Liu, Rixiang Quan, Sergio Cantero Chinchilla
Supervision: Fengyuan Liu
Writing-original draft: Rixiang Quan
Writing-review & editing: Fengyuan Liu, Sergio Cantero Chinchilla

Ethics approval and consent to participate

Not applicable.

Consent for publication

Not applicable.

Availability of data

The complete implementation of the proposed framework will publicly be available on GitHub (https://github.com/davidquanaa/FEANN-Print), including data processing pipelines, model code, and finite element analysis (FEA) coupling scripts. To support reproducibility and promote

broader adoption, we have prepared a companion software article—to be submitted to SoftwareX—titled: *FEANN-Print: A Coupled ANN and FEA Framework for Enhanced Prediction and Design of 3D-Printed Bone Scaffolds*, which provides comprehensive documentation of the framework's architecture and functionality.

Further disclosure

A portion of this work (title: Machine Learning-Driven Optimization of 3D Printing Parameters for PLA Bone Scaffolds with Enhanced Mechanical Properties) was presented at the 6th CIRP Conference (Dresden, Germany) in June 2024.

References

1. O'Brien FJ. Biomaterials and scaffolds for tissue engineering. *Mater Today.* 2011;14(3):88-95. doi: 10.1016/S1369-7021(11)70058-X
2. Hutmacher DW. Scaffolds in tissue engineering bone and cartilage. *Biomaterials.* 2000;21(24):2529-2543. doi: 10.1016/S0142-9612(00)00121-6
3. Bose S, Roy M, Bandyopadhyay A. Recent advances in bone tissue engineering scaffolds. *Trends Biotechnol.* 2012;30(10):546-554. doi: 10.1016/j.tibtech.2012.07.005
4. Feng Y, Zhu S, Mei D, *et al*. Application of 3D printing technology in bone tissue engineering: a review. *Curr Drug Deliv.* 2021;18:847-861. doi: 10.2174/1567201817999201113100322
5. Xu Y, Zhang F, Zhai W, Cheng S, Li J, Wang Y. Unraveling of advances in 3D-printed polymer-based bone scaffolds. *Polymers (Basel).* 2022;14:566. doi: 10.3390/polym14030566
6. Hussain M, Khan SM, Shafiq M, Abbas N. A review on PLA-based biodegradable materials for biomedical applications. *Giant.* 2024;18(3):100261. doi: 10.1016/j.giant.2024.100261
7. Afonso J, Alves JL, Caldas G, Gouveia BP, Santana L, Belinha J. Influence of 3D printing process parameters on the mechanical properties and mass of PLA parts and predictive models. *Rapid Prototyp J.* 2021;27(3):487-495. doi: 10.1108/RPJ-03-2020-0043
8. Ma S, Tang Q, Liu Y, Feng Q. Prediction of mechanical properties of three-dimensional printed lattice structures through machine learning. *J Comput Inf Sci Eng.* 2022;22(3):031008. doi: 10.1115/1.4053077
9. Sheoran AJ, Kumar H. Fused deposition modeling process parameters optimization and effect on mechanical properties and part quality: review and reflection on present research. *Mater Today Proc.* 2020;21:1659-1672. doi: 10.1016/j.matpr.2019.11.296
10. Goh GD, Sing SL, Yeong WY. A review on machine learning in 3D printing: applications, potential, and challenges. *Artif Intell Rev.* 2021;54(1):63-94. doi: 10.1007/s10462-020-09876-9
11. Goh GD, Sing SL, Lim YF, *et al*. Machine learning for 3D-printed multi-materials tissue-mimicking anatomical models. *Mater Des.* 2021;211:110125. doi: 10.1016/j.matdes.2021.110125
12. Jayasudha M, Elangovan M, Mahdal M, Priyadarshini J. Accurate estimation of tensile strength of 3D-printed parts using machine learning algorithms. *Processes.* 2022;10(6):1158. doi: 10.3390/pr10061158
13. Rodrigues JF, Florea L, de Oliveira MC, Diamond D, Oliveira ON. Big data and machine learning for materials science. *Discover Mater.* 2021;1:1-27. doi: 10.1007/s43939-021-00012-0
14. Oviedo F, Ferres JL, Buonassisi T, Butler KT. Interpretable and explainable machine learning for materials science and chemistry. *Acc Mater Res.* 2022;3(6):597-607. doi: 10.1021/accountsmr.1c00244
15. Kalina KA, Linden L, Brummund J, Kästner M. FE-ANN: an efficient data-driven multiscale approach based on physics-constrained neural networks and automated data mining. *Comput Mech.* 2023;71(5):827-851. doi: 10.1007/s00466-022-02260-0
16. Peng B, Wei Y, Qin Y, *et al*. Machine learning-enabled constrained multi-objective design of architected materials. *Nat Commun.* 2023;14(1):6630. doi: 10.1038/s41467-023-42415-y
17. Oladipo B, Matos H, Krishnan NA, Das SJ. Integrating experiments, finite element analysis, and interpretable machine learning to evaluate the auxetic response of 3D-printed re-entrant metamaterials. *J Mater Res Technol.* 2023;25:1612-1625. doi: 10.1016/j.jmrt.2023.06.038
18. Drakoulas G, Gortsas T, Polyzos E, *et al*. An explainable machine learning-based probabilistic framework for the design of scaffolds in bone tissue engineering. *Biomech Model Mechanobiol.* 2024;23(3):987-1012. doi: 10.1007/s10237-024-01817-7
19. Dong H, Liu F, Ye L, *et al*. Process optimization and mechanical property investigation of Inconel 718 manufactured by selective electron beam melting. *Mater Sci Addit Manuf.* 2022;1(4):23. doi: 10.18063/msam.v1i4.23
20. Rodrigues N, Benning M, Ferreira AM, Dixon L, Dalgarno K. Manufacture and characterisation of porous PLA scaffolds. *Procedia CIRP.* 2016;49:33-38. doi: 10.1016/j.procir.2015.07.025

21. Frunzaverde D, Cojocaru V, Ciubotariu CR, *et al*. The influence of the printing temperature and the filament color on the dimensional accuracy, tensile strength, and friction performance of FFF-printed PLA specimens. *Polymers (Basel)*. 2022;14(10):1978.
doi: 10.3390/polym14101978

22. Lei M, Wei Q, Li M, Zhang J, Yang R, Wang Y. Numerical simulation and experimental study of the effects of process parameters on filament morphology and mechanical properties of FDM 3D-printed PLA/GNPs nanocomposite. *Polymers (Basel)*. 2022; 14(15):3081.
doi: 10.3390/polym14153081

23. Wickramasinghe S, Do T, Tran P. FDM-based 3D printing of polymer and associated composite: a review on mechanical properties, defects, and treatments. *Polymers (Basel)*. 2020;12(7):1529.
doi: 10.3390/polym12071529

24. Heidari-Rarani M, Ezati N, Sadeghi P, Badrossamay M. Optimization of FDM process parameters for tensile properties of polylactic acid specimens using Taguchi design of experiment method. *J Thermoplast Compos Mater*. 2022;35(12):2435-2452.
doi: 10.1177/0892705720964560

25. Chokshi H, Shah DB, Patel KM, Joshi SJ. Experimental investigations of process parameters on mechanical properties for PLA during processing in FDM. *Adv Mater Process Technol*. 2022;8(suppl 2):696-709.
doi: 10.1080/2374068X.2021.1946756

26. Farah S, Anderson DG, Langer R. Physical and mechanical properties of PLA and their functions in widespread applications—a comprehensive review. *Adv Drug Deliv Rev*. 2016;107:367-392.
doi: 10.1016/j.addr.2016.06.012

27. Zienkiewicz OC, Taylor RL, Zhu JZ. Chapter 10: Incompressible problems, mixed methods, and other procedures of solution. In: *The Finite Element Method: Its Basis and Fundamentals*. 7th ed.; 2013:315-359.
doi: 10.1016/B978-1-85617-633-0.00010-1

28. Gomes MS, Carmo GP, Ptak M, Fernandes FA, Alves de Sousa RJ. Accuracy and efficiency of finite element head models: the role of finite element formulation and material laws. *Int J Numer Methods Biomed Eng*. 2024;40(9):e3851.
doi: 10.1002/cnm.3851

29. Zienkiewicz OC, Taylor RL, Zhu JZ. Chapter 16: Adaptive finite element refinement. In: *The Finite Element Method: Its Basis and Fundamentals*. 7th ed.; 2013:545-572.
doi: 10.1016/B978-1-85617-633-0.00016-2

30. Demir M, Seki Y. Interfacial adhesion strength between FDM-printed PLA parts and surface-treated cellulosic-woven fabrics. *Rapid Prototyp J*. 2023;29(6):1166-1174.
doi: 10.1108/RPJ-10-2022-0369

31. Rankouhi B, Javadpour S, Delfanian F, Letcher T. Failure analysis and mechanical characterization of 3D-printed ABS with respect to layer thickness and orientation. *J Fail Anal Prev*. 2016;16(3):467-481.
doi: 10.1007/s11668-016-0113-2

32. Sagias V, Giannakopoulos K, Stergiou C. Mechanical properties of 3D-printed polymer specimens. *Procedia Struct Integr*. 2018;10:85-90.
doi: 10.1016/j.prostr.2018.09.013

33. Xu L, Leguillon D. Dual-notch void model to explain the anisotropic strengths of 3D-printed polymers. *J Eng Mater Technol*. 2020;142(3):031001.
doi: 10.1115/1.4044282

34. Ahn SH, Montero M, Odell D, Roundy S, Wright PK. Anisotropic material properties of fused deposition modeling ABS. *Rapid Prototyp J*. 2002;8(4):248-257.
doi: 10.1108/13552540210441166

35. Chen J, Liu X, Tian Y, *et al*. 3D-printed anisotropic polymer materials for functional applications. *Adv Mater*. 2022;34(5):2102877.
doi: 10.1002/adma.202102877

36. Castelló-Pedrero P, García-Gascón C, García-Manrique J. Multiscale numerical modeling of large-format additive manufacturing processes using carbon fiber reinforced polymer for digital twin applications. *Int J Mater Form*. 2024;17(2):15.
doi: 10.1007/s12289-024-01811-5

37. He K, Zhang X, Ren S, Sun J. Delving deep into rectifiers: surpassing human-level performance on ImageNet classification. In: *Proceedings of the IEEE International Conference on Computer Vision (ICCV);* 2015: 1026-1034.
doi: 10.1109/ICCV.2015.123

38. Varma S, Simon R. Bias in error estimation when using cross-validation for model selection. *BMC Bioinformatics*. 2006;7(1):91.
doi: 10.1186/1471-2105-7-91

39. Banerjee S, Lio P, Jones PB, Cardinal RN. A class-contrastive human-interpretable machine learning approach to predict mortality in severe mental illness. *npj Schizophr*. 2021;7(1):60.
doi: 10.1038/s41537-021-00191-y

40. Schnaubelt M. A comparison of machine learning model validation schemes for non-stationary time series data. Preprint. 2019.

41. Glorot X, Bordes A, Bengio Y. Deep sparse rectifier neural networks. In: JMLR Workshop Conf Proc. 2011;315-323.

42. Vakalopoulou M, Christodoulidis S, Burgos N, Colliot O, Lepetit VJ. Deep Learning: Basics and Convolutional Neural Networks (CNNs); 2023:77-115.
doi: 10.1007/978-1-0716-3195-9_3

43. Cantero-Chinchilla S, Simpson CA, Ballisat A, Croxford AJ, Wilcox PD. Convolutional neural networks for ultrasound corrosion profile time series regression. *NDT E Int*. 2023;133:102756. doi: 10.1016/j.ndteint.2022.102756

44. Rahaman R, Thiery AH. Uncertainty quantification and deep ensembles. *Adv Neural Inf Process Syst*. 2021;34:20063-20075. doi: 10.48550/arXiv.2007.08792

45. Ovadia Y, Fertig E, Ren J, *et al*. Can you trust your model's uncertainty? Evaluating predictive uncertainty under dataset shift. *Adv Neural Inf Process Syst*. 2019;32. doi: 10.48550/arXiv.1906.02530

46. Fort S, Hu H, Lakshminarayanan B. Deep ensembles: a loss landscape perspective. In: International Conference on Learning Representations (ICLR); 2020. doi: 10.48550/arXiv.1912.02757

47. Pepelnjak T, Sevšek L, Movrin D, Milutinović M. Influence of process parameters on the characteristics of additively manufactured parts made from advanced biopolymers. *Polymers (Basel)*. 2023;15(3):716. doi: 10.3390/polym15030716

48. Wang C, Tan XP, Tor SB, Lim CJ. Machine learning in additive manufacturing: state-of-the-art and perspectives. *Addit Manuf*. 2020;36:101538. doi: 10.1016/j.addma.2020.101538

49. Wu H, Sulkis M, Driver J, Saade-Castillo A, Thompson A, Koo JH. Multi-functional ULTEM™ 1010 composite filaments for additive manufacturing using fused filament fabrication (FFF). *Addit Manuf*. 2018;24:298-306. doi: 10.1016/j.addma.2018.10.014

50. Zhao X, Li S, Zhang M, *et al*. Comparison of the microstructures and mechanical properties of Ti–6Al–4V fabricated by selective laser melting and electron beam melting. *Mater Des*. 2016;95:21-31. doi: 10.1016/j.matdes.2015.12.135

51. Dejene ND, Lemu HG. Characterisation and prediction of mechanical properties in laser powder bed fusion-printed parts: a comparative analysis using machine learning. *Mater Tehnol*. 2024;39(1):2419228. doi: 10.1080/10667857.2024.2419228

52. Ibrahimi S, D'Andrea L, Gastaldi D, Rivolta MW, Vena P. Machine learning approaches for the design of biomechanically compatible bone tissue engineering scaffolds. *Comput Methods Appl Mech Eng*. 2024;423:116842. doi: 10.1016/j.cma.2024.116842

53. Rudolph M, Kurz S, Rakitsch J. Hybrid modeling design patterns. *J Math Ind*. 2024;14(1):3. doi: 10.1186/s13362-024-00141-0

54. Lamane H, Mouhir L, Moussadek R, Baghdad B, Kisi O, El Bilali A. Interpreting machine learning models based on SHAP values in predicting suspended sediment concentration. *Int J Sediment Res*. 2025;40(1):91-107. doi: 10.1016/j.ijsrc.2024.10.002

55. Lundberg SM, Lee SI. A unified approach to interpreting model predictions. *Adv Neural Inf Process Syst*. 2017;30. doi: 10.48550/arXiv.1705.07874

56. Rooks NB, Besier TF, Schneider MT. A parameter sensitivity analysis on multiple finite element knee joint models. *Front Bioeng Biotechnol*. 2022;10:841882. doi: 10.3389/fbioe.2022.841882

57. Gal Y, Ghahramani Z. Dropout as a Bayesian Approximation: Representing Model Uncertainty in Deep Learning. In: Proceedings of the 33rd International Conference on Machine Learning (ICML 2016). *Proc Mach Learn Res*. 2016;48:1050-1059. https://proceedings.mlr.press/v48/gal16.html

58. Kendall A, Gal Y. What uncertainties do we need in Bayesian deep learning for computer vision? *Adv Neural Inf Process Syst*. 2017;30:5575-5585.

59. Bock FE, Keller S, Huber N, Klusemann B. Hybrid modelling by machine learning corrections of analytical model predictions towards high-fidelity simulation solutions. *Materials (Basel)*. 2021;14(8):1883. doi: 10.3390/ma14081883

60. Aldakheel F, Elsayed ES, Heider Y, Weeger O. Physics-based machine learning for computational fracture mechanics. *Mach Learn Comput Sci Eng*. 2025;1(1):18. doi: 10.1007/s44379-025-00019-x

61. Napolitano F, Cozzolino E, Papa I, Astarita A, Squillace A. Experimental integrated approach for mechanical characteristic optimization of FDM-printed PLA in an energy-saving perspective. *Int J Adv Manuf Technol*. 2022;121(5):3551-3565. doi: 10.1007/s00170-022-09535-z

62. Yao H, Gao Y, Liu Y. FEA-Net: A physics-guided data-driven model for efficient mechanical response prediction. *Comput Methods Appl Mech Eng*. 2020;363:112892. doi: 10.1016/j.cma.2020.112892

63. Bahraminasab M. Challenges on optimization of 3D-printed bone scaffolds. *BioMed Eng Online*. 2020;19(1):69. doi: 10.1186/s12938-020-00810-2

64. Akbari P, Zamani M, Mostafaei A. Machine learning prediction of mechanical properties in metal additive manufacturing. *Addit Manuf*. 2024;91:104320. doi: 10.1016/j.addma.2024.104320

65. Ng WL, Goh GL, Goh GD, Ten JSJ, Yeong WY. Progress and opportunities for machine learning in materials and processes of additive manufacturing. *Adv Mater*. 2024;36(34):2310006. doi: 10.1002/adma.202310006

66. Mohamed AP, Lee B, Zhang Y, *et al*. Simulation-enhanced data augmentation for machine learning pathloss prediction. In: ICC 2024 - IEEE International Conference on Communications; 2024: 4863-4868.